RSC Advances

ROYAL SOCIETY OF CHEMISTRY

PAPER

View Article Online
View Journal | View Issue

Cite this: *RSC Adv.*, 2025, **15**, 44893

Synthesis and application of Fe/Ni modified ZIF-8 as an environmentally friendly photocatalyst for methylene blue dye degradation under visible light

Siti Saenab,[a] Oka Pradipta Arjasa,[b] Fajar Inggit Pambudi *[a] and Dwi Siswanta [a]

A series of Fe(III) and Ni(II) bimetallic doped ZIF-8 materials were synthesized *via* a facile, green, room-temperature method to act as highly efficient photocatalysts for methylene blue (MB) degradation. The study reveals that the Fe/Ni bimetallic synergistic effect is crucial for enhancing photocatalytic performance. Optimization of the metal doping ratio revealed that Fe(15)/Ni(5)@ZIF-8 exhibited the highest photocatalytic efficiency. This optimized catalyst maintained the parent ZIF-8 crystalline structure but showed an increased particle size (80 nm). X-ray Photoelectron Spectroscopy (XPS) confirmed the successful metal incorporation and, importantly, the presence of mixed valence states for both iron (Fe^{2+}/Fe^{3+}) and nickel (Ni^{2+}/Ni^{3+}). This electronic modification leads to a significant reduction of the material's band gap to 2.26 eV, enabling strong visible light absorption. Consequently, the optimized photocatalyst exhibited outstanding activity, achieving 95.06% degradation of MB within 180 minutes under visible light, following pseudo-first-order kinetics ($k = 2.73 \times 10^{-2}$ min^{-1}). This work not only presents a highly stable and effective catalyst but also underscores that harnessing bimetallic synergy is a powerful strategy for engineering advanced MOF-based materials for environmental remediation.

Received 4th August 2025
Accepted 6th November 2025

DOI: 10.1039/d5ra05662d

rsc.li/rsc-advances

Introduction

The rapid development of the textile industry has significantly contributed to the global economy through job creation and economic growth. Nevertheless, this progress has simultaneously posed serious environmental concerns. Intensive use of synthetic dyes and various chemical reagents in textile production,[1] along with the discharge of untreated wastewater from textile, paint, plastic, agricultural, and dyeing industries, has led to severe water contamination. Synthetic dyes, being stable organic pollutants, exhibit high resistance to natural degradation and persist in aquatic environments, thereby impeding light penetration and reducing dissolved oxygen levels essential for aquatic organisms.[2] Although various treatment technologies—physical, chemical, and biological—have been proposed, most still produce toxic by-products that may lead to secondary pollution.[3]

In response to the limitations of conventional wastewater treatment methods, catalytic photodegradation has emerged as a more environmentally friendly and efficient approach for the removal of dyes from wastewater.[4–7] This "green" technique employs photocatalytic oxidation processes activated by ultraviolet (UV) or visible (Vis) light to cleave the chromophoric structures of dyes, achieving complete mineralization into non-toxic end products such as CO_2 and H_2O.[8] However, traditional photocatalytic materials, including metal oxides and sulfides, often suffer from high recombination rates of photogenerated charge carriers, which significantly reduce their photocatalytic efficiency.[9] These drawbacks have prompted the exploration of novel materials with enhanced charge separation and photocatalytic activity. With the advancement of materials science, various emerging candidates—such as metal–organic frameworks (MOFs), covalent organic frameworks (COFs), zeolites, activated carbon, and nanoparticles—have been extensively developed to improve photocatalytic performance through structural engineering and electronic property optimization.

Metal–organic frameworks (MOFs) are crystalline porous materials composed of metal ions or metal clusters interconnected by organic linkers. Their unique architectures enable photocatalytic activity through ligand-to-metal charge transfer (LMCT) processes, facilitated by the electronic configuration between the highest occupied molecular orbital (HOMO) and the lowest unoccupied molecular orbital (LUMO).[10,11] MOFs possess several remarkable advantages, including tunable pore sizes and exceptionally high surface areas, making them promising candidates for photocatalytic applications.[3] Among various MOF derivatives, zeolitic imidazolate frameworks (ZIFs) have attracted considerable attention for combining zeolitic characteristics with metal–organic coordination features. ZIFs

[a]*Department of Chemistry, Universitas Gadjah Mada, Sekip Utara, 55281 Yogyakarta, Indonesia. E-mail: fajar.inggit@ugm.ac.id*

[b]*Advanced Materials Research Centre – National Research and Innovation Agency, Banten 15314, Indonesia*

consist of transition metal ions, such as Zn(II) or Co(II), coordinated with imidazolate linkers to form a three-dimensional tetrahedral framework.[12] These materials are highly appealing due to their large surface areas, excellent crystallinity, and outstanding thermal and chemical stability.[13] One of the most extensively studied members, ZIF-8, exhibits superior chemical and thermal stability compared with other MOFs.[14] However, ZIF-8 possesses a relatively wide band gap (~5 eV) owing to the intrinsic electronic properties of its imidazolate rings.[15] The strong absorption peak observed around 230 nm originates from the $\pi \rightarrow \pi^*$ transition within the imidazolate structure, involving electron excitation from the HOMO to the LUMO, which requires high energy due to the large energy difference between these orbitals.[15] Consequently, the photocatalytic activity of pristine ZIF-8 under visible light irradiation remains limited, necessitating optical modification to enhance its photodegradation performance.

To overcome these limitations, various strategies have been developed through structural modification, particularly *via* metal ion doping or substitution, which can alter the morphology, optical properties, and structural characteristics of the material, thereby enhancing its photocatalytic activity. Bimetallic MOFs generally exhibit superior performance compared to their monometallic counterparts due to the synergistic interactions between metal ions that facilitate metal-to-metal charge transfer (MMCT).[16,17] Abdi (2020)[17] successfully synthesized Ag-doped ZIF-8, which demonstrated a significant improvement in the degradation efficiency of dyes such as methyl orange and rhodamine B, where Ag ions acted as electron traps that promoted charge separation. Thanh *et al.* reported that Fe doping in ZIF-8 induced a red shift and narrowed the band gap, resulting in enhanced photocatalytic activity toward the degradation of Remazol Deep Blue under sunlight irradiation. In Fe-ZIF-8, the Fe valence orbitals elevate the HOMO energy level, extending light absorption into the visible region and facilitating more efficient charge transfer.[15] Similarly, Mphuthi *et al.* found that Fe(II)-incorporated ZIF-8 nanoparticles achieved up to 98% degradation efficiency of Remazol Brilliant Blue R (RBBR) after 120 minutes of visible light irradiation, with a rate constant of 2.20×10^{-2} min^{-1}.[18] Furthermore, Zulfa *et al.* confirmed that Ni doping in ZIF-8 led to a narrower band gap and lower charge recombination rate than pristine ZIF-8, achieving 93.22% methylene blue degradation within 150 minutes under UV illumination. The corrosion-resistant nature of Ni also provides additional stability in the photocatalytic system.[11]

Previous studies have demonstrated that single-ion doping of Fe or Ni into ZIF-8 can enhance photocatalytic activity by extending light absorption and suppressing electron–hole recombination.[19,20] However, the simultaneous incorporation of Fe and Ni ions into ZIF-8 for the photocatalytic degradation of methylene blue (MB) under visible light irradiation has not yet been reported, particularly through an environmentally friendly synthesis route. The integration of these two metals is expected to generate a synergistic effect between the redox properties of Fe and the chemical stability of Ni.[11,18] The presence of these metal ions can modify the surface characteristics of ZIF-8, creating a more active charge distribution and increasing the number of adsorption sites. Such modifications strengthen the interaction between the catalyst surface and MB molecules through electrostatic attraction, π–π interactions, and hydrogen bonding.[21] Moreover, the coexistence of Fe and Ni can facilitate metal-to-metal charge transfer (MMCT) among Fe–N, Ni–N, and Zn–N clusters, collectively enhancing charge separation and improving photocatalytic degradation efficiency.[22]

Materials and methods

Chemicals and reagents

The primary materials employed in this research consisted of zinc(II) nitrate hexahydrate ($Zn(NO_3)_2 \cdot 6H_2O$) (Merck, 99%), nickel(II) nitrate hexahydrate ($Ni(NO_3)_2 \cdot 6H_2O$) (Merck, 99%), iron(III) nitrate nonahydrate ($Fe(NO_3)_3 \cdot 9H_2O$) (Merck, 99%), 2-methylimidazole (Merck, 99%), and ascorbic acid (Merck, 99%). The supporting materials utilized included triethylamine (Sigma-Aldrich, 99%), methanol (Sigma-Aldrich, 99.9%), methylene blue (Sigma-Aldrich, 99%), isopropyl alcohol (Sigma-Aldrich, 99.7%), dimethyl sulfoxide (Sigma-Aldrich, 99.8%), and deionized water (Onemed; Indonesia).

Synthesis of ZIF-8, Fe@ZIF-8, Ni@ZIF-8 and Fe/Ni@ZIF-8

The synthesis procedure of ZIF-8, single metal doped (Fe or Ni), and its bimetallic (Fe/Ni) variants was adapted from a previously reported method with slight modifications.[11] Typically, 3.375 mmol of metal precursors ($Zn(NO_3)_2 \cdot 6H_2O$, $Fe(NO_3)_3 \cdot 9H_2O$ and/or $Ni(NO_3)_2 \cdot 6H_2O$) with Zn : Fe : Ni molar ratios of 100 : 0 : 0, 80 : 20 : 0, 80 : 0 : 20, 80 : 5 : 15, 80 : 10 : 10, and 80 : 15 : 5 were dissolved in 7.5 mL deionized water. Separately, 27 mmol of 2-methylimidazole was dissolved in a mixture of 3.9 mL of triethylamine and 7.5 mL of deionized water. Both solutions were sonicated for 10 min, after which the metal solution was added dropwise to the ligand solution under continuous stirring (500 rpm). The mixture was stirred for an additional 60 min and then aged at room temperature for 24 h. The resulting precipitate was collected by centrifugation (5000 rpm, 10 min), washed three times with deionized water and twice with methanol, and dried at 60 °C overnight. The obtained samples were denoted as ZIF-8, Fe@ZIF-8, Ni@ZIF-8, Fe(5)/Ni(15)@ZIF-8, Fe(10)/Ni(10)@ZIF-8, and Fe(15)/Ni(5)@ZIF-8.

Characterization

The crystalline phases of ZIF-8 and metal-doped ZIF-8 photocatalysts were characterized by high-resolution X-ray diffraction (XRD, Empyrean, PANalytical, Netherlands) equipped with Thin Film Metrology and SAXS, using Cu-Kα radiation ($\lambda = 1.54060$ Å) in the 2θ range of 5–50°. Functional groups were identified by Fourier-transform infrared spectroscopy (FTIR, IR Prestige-21, Shimadzu, Japan) in the range of 400–4000 cm^{-1}. The morphology and elemental distribution of the samples were observed using field-emission scanning electron microscopy with energy-dispersive X-ray spectroscopy (FESEM-EDX, JSM-IT700HR, JEOL, Japan). Optical properties were assessed *via*

diffuse reflectance UV-Vis spectroscopy (DR-UV, Lambda 365+, PerkinElmer, USA). X-ray photoelectron spectroscopy (XPS, Axis Supra+, Kratos Analytical Ltd, UK) was employed to analyze the chemical bonding states of Fe(15)/Ni(5)@ZIF-8. Methylene blue (MB) concentrations after photodegradation were quantified using a UV-Vis spectrophotometer (Orion AquaMate 8100, Thermo Scientific, USA). All measurements were conducted under ambient conditions.

Photocatalytic activity measurements

The photocatalytic performance of the synthesized materials was evaluated through the degradation of methylene blue (MB) under visible light irradiation at ambient temperature. Prior to the degradation tests, the photocatalysts were thermally activated at 60 °C for 24 h in an oven. To determine the adsorption–desorption equilibrium, 10 mg of each photocatalyst (ZIF-8, single metal doped, and Fe/Ni@ZIF-8) was dispersed in 10 mL of MB solution (30 mg L^{-1}, pH ≈ 6.8), followed by stirring in the dark for various contact times (15, 30, 45, 60, and 75 min). The optimal equilibrium time was subsequently used as the pre-irradiation equilibration period for all photocatalytic runs.

Photodegradation experiments were carried out under visible light irradiation provided by four 20 W Philips tungsten lamps placed equidistantly around the reaction vessel. The photocatalyst–dye mixture was irradiated for specific time intervals of 5, 10, 15, 30, 60, and up to 180 min. At each interval, aliquots were withdrawn, centrifuged at 5000 rpm for 10 min to remove particulates, and the concentration of MB was analyzed by UV-Vis spectrophotometry at a wavelength of 664 nm. The photocatalyst exhibiting the highest degradation activity was subsequently employed to evaluate the photocatalytic efficiency under various conditions, including different initial pH values, catalyst dosages, and initial dye concentrations.

The Fe(15)/Ni(5)@ZIF-8 composite was assessed for stability and recyclability through three consecutive runs of MB degradation under identical conditions (30 mg per L MB, 10 mL solution, 10 mg catalyst, 180 min irradiation). After each run, the photocatalyst was washed with methanol and dried at 60 °C before reuse. Reactive species involved in the degradation were examined *via* trapping experiments using IPA ($\cdot OH$), DMSO (e^-), ascorbic acid ($\cdot O_2^-$), and EDTA (h^+) as scavengers under identical conditions.

Result and discussion

Morphological and structural properties

XRD. The phase purity and crystallinity of the pristine ZIF-8, single-doped (Fe or Ni), and co-doped Fe/Ni@ZIF-8 composites were further examined by X-ray diffraction (XRD) analysis. In addition, the synthesized photocatalyst powders are provided in Fig. S1 of the SI with their respective colour. In Fig. 1, all samples exhibited diffraction patterns that closely matched the characteristic peaks of the sodalite (SOD)-type ZIF-8 structure, as reported from Yaghi *et al.*[23] The major diffraction peaks were observed at 2θ = 7.29° (110) and 12.69° (211) with high intensity, along with additional peaks at 2θ = 10.39° (200), 16.38° (310), and 17.96° (222), showing low to moderate intensity levels. Although no significant shift in peak positions was observed, a gradual decrease in peak intensity was noted in Fe@ZIF-8, Ni@ZIF-8, Fe(5)/Ni(15)@ZIF-8, Fe(10)/Ni(10)@ZIF-8, and Fe(15)/Ni(5)@ZIF-8, indicating a reduction in crystallinity due to metal doping. This phenomenon is attributed to the competitive coordination between Fe/Ni and Zn ions toward the nitrogen atoms in the imidazolate ligands. Notably, Fe exhibits a stronger interaction with nitrogen lone pairs than Zn, which is consistent with its higher electronegativity value (1.85 for Fe *versus* 1.65 for Zn).[15]

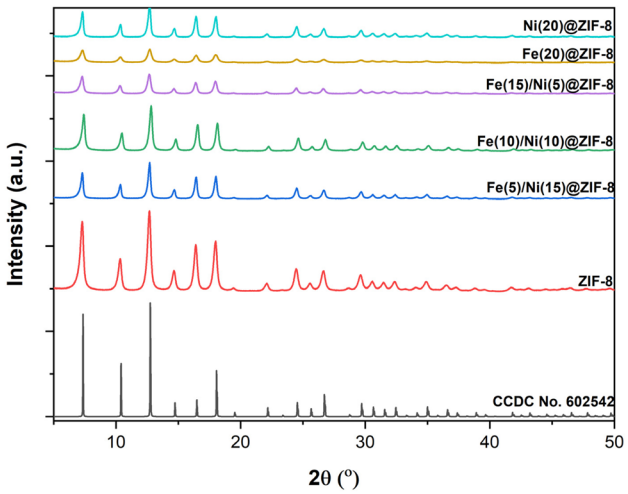

Fig. 1 XRD pattern of ZIF-8 reference, ZIF-8, Fe(5)/Ni(15)@ZIF-8, Fe(10)/Ni(10)@ZIF-8, Fe(15)/Ni(5)@ZIF-8, Fe@ZIF-8, and Ni@ZIF-8.

To further investigate potential changes in the crystal lattice, Le Bail refinement was applied to the experimental XRD data. This method involved the fitting of experimental diffraction patterns to the reference unit cell and space group parameters of ZIF-8, which crystallizes in a cubic system (space group $I\bar{4}3m$) with orthogonal lattice angles of 90°, as shown in Fig. S2. The refinement results, presented in Table 1, demonstrate that the incorporation of Fe and Ni did not significantly alter the unit cell parameters. This suggests that the dopant metals were successfully integrated into the ZIF-8 framework without disrupting its crystalline topology. The retention of peak positions and overall pattern alignment with the standard ZIF-8 also confirms the absence of secondary phases or detectable impurities, indicating that the synthesized materials remain phase-pure.[15]

FTIR. Fourier Transform Infrared (FTIR) spectroscopy was employed to identify the functional groups and to investigate possible bond alterations in the ZIF-8 framework upon doping with Fe and Ni metals at various molar ratios, as illustrated in Fig. 2. In the FTIR spectrum of pristine ZIF-8, the characteristic vibrations of the 2-methylimidazolate ligand can be observed in several absorption bands. An absorption band at 2928 cm^{-1} is attributed to the asymmetric stretching vibration of the C–H bond in methyl groups ($-CH_3$). The aliphatic C–H stretching vibration is observed at around 1400 cm^{-1}. Additionally, a weak band at 1143 cm^{-1} indicates the presence of C–N stretching vibrations associated with the aliphatic ring of the ligand.[17,24]

Table 1 Lattice parameter changes of ZIF-8 and Fe/Ni@ZIF-8 composite

Photocatalyst	Space group	$a = b = c$ (Å)	Cell volume (Å^3)	R_w (%)
ZIF-8	$I\bar{4}3m$	17.016(5)	4927.310(4)	7.748
Fe(5)/Ni(15)@ZIF-8	$I\bar{4}3m$	17.004(3)	4916.438(2)	6.861
Fe(10)/Ni(10)@ZIF-8	$I\bar{4}3m$	16.980(5)	4896.025(5)	9.781
Fe(15)/Ni(5)@ZIF-8	$I\bar{4}3m$	17.018(5)	4928.523(4)	9.189

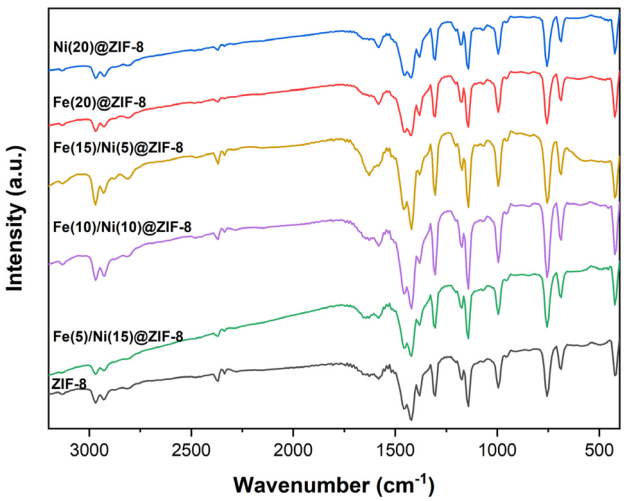

Fig. 2 FTIR spectra of ZIF-8, single doped Fe@ZIF-8 and Ni@ZIF-8, and Fe/Ni@ZIF-8 composites.

Sharp absorption bands observed in the region of 690–900 cm^{-1} are indicative of aromatic C–H bending vibrations from the imidazole ring. Furthermore, the absorption band at 424 cm^{-1} is assigned to the Zn–N stretching mode, which is a key structural component of the ZIF-8 framework.[25] The FTIR spectra of Fe/Ni-modified ZIF-8 composites exhibit similar absorption features to those of pristine ZIF-8, indicating that the basic framework of ZIF-8 is retained after metal doping.[26]

FESEM-EDX mapping. Field Emission Scanning Electron Microscopy (FESEM) combined with EDX mapping was conducted to examine the effect of Fe and Ni doping on the surface morphology and elemental composition of the Fe/Ni@ZIF-8 photocatalyst. The FESEM images of pristine ZIF-8 and its Fe/Ni-modified composites with varying metal ratios are presented in Fig. 3. The pristine ZIF-8 sample (Fig. 3(a)) exhibited a relatively uniform crystal morphology with small particle sizes and homogeneous distribution. Upon co-doping with Fe and Ni, notable morphological changes were observed. The Fe(5)/Ni(15)@ZIF-8 sample (Fig. 3(b)) displayed larger particle sizes and less uniform morphology compared to the undoped ZIF-8. Further increase in metal content, as seen in Fe(10)/Ni(10)@ZIF-8 (Fig. 3(c)) and Fe(15)/Ni(5)@ZIF-8 (Fig. 3(d)), led to pronounced particle agglomeration. This agglomeration is likely attributed to increased surface energy and enhanced van der Waals interactions among the particles due to their high surface area.[27] Such morphological evolution may influence the photocatalytic behavior by affecting the active surface sites, charge transport, and light absorption characteristics of the materials.

The particle size distribution analysis confirmed that the incorporation of Fe and Ni metals led to an increase in the average particle size from approximately 50 nm in pristine ZIF-8 to around 80 nm in the Fe/Ni@ZIF-8 composites. Such variations can be attributed to differences in synthetic conditions that affect the nucleation and crystal growth kinetics. The presence of Fe^{3+} and Ni^{2+} ions may act as heterogeneous nucleation sites, thereby altering the crystallization mechanism. Moreover, the partial substitution of metal ions alters the interaction with 2-methylimidazole ligands and modifies the deprotonation rate, which slows down nucleation and allows for the formation of larger crystals.[27]

The EDX elemental mapping results, shown in Fig. 4, provided insights into the surface elemental distribution. The pristine ZIF-8 sample (Fig. 4(a)) exhibited a homogeneous distribution of Zn, C, and N, consistent with the well-defined framework of the parent structure. Zn is primarily concentrated at the metal nodes of the MOF structure, while C and N are distributed along the organic linkers. In Fe(5)/Ni(15)@ZIF-8 (Fig. 4(b)), both Fe and Ni were relatively well-dispersed throughout the framework, with a notably higher intensity of Ni, which suggest its potential role as a stabilizing agent that minimizes particle agglomeration.[28] The sample Fe(10)/Ni(10)@ZIF-8 (Fig. 4(c)) exhibited localized enrichment of Fe and Ni, suggesting the possible formation of Fe/Ni clusters. In contrast, Fe(15)/Ni(5)@ZIF-8 (Fig. 4(d)) showed a dominant accumulation of Fe with a more limited distribution of Ni.

Quantitative data obtained from EDX and XRF analyses are presented in Table 2. The Zn content, designed to be approximately 80 wt%, was successfully achieved, with experimental values ranging from 78.34% to 83.2%, indicating good agreement with the theoretical composition. This confirms the effective incorporation of Fe and Ni into the ZIF-8 framework, most likely *via* partial substitution or surface deposition, without inducing significant structural disruption. The Fe content increased from 5.38% to 12.5%, while the Ni content decreased from 11.48% to 4.55%, consistent with the molar ratios of the dopant precursors. The strong correlation between EDX and XRF results supports the reliability of the compositional data and further confirms the successful immobilization of Fe and Ni within the host structure.

SAA. The N_2 adsorption–desorption isotherms were employed to determine the specific surface area (S_{BET}) of pristine ZIF-8, Fe(5)/Ni(15)@ZIF-8, Fe(10)/Ni(10)@ZIF-8, and Fe(15)/Ni(5)@ZIF-8, as shown in Fig. S3 and pore size distribution are presented in Table 3. All samples exhibited type I adsorption

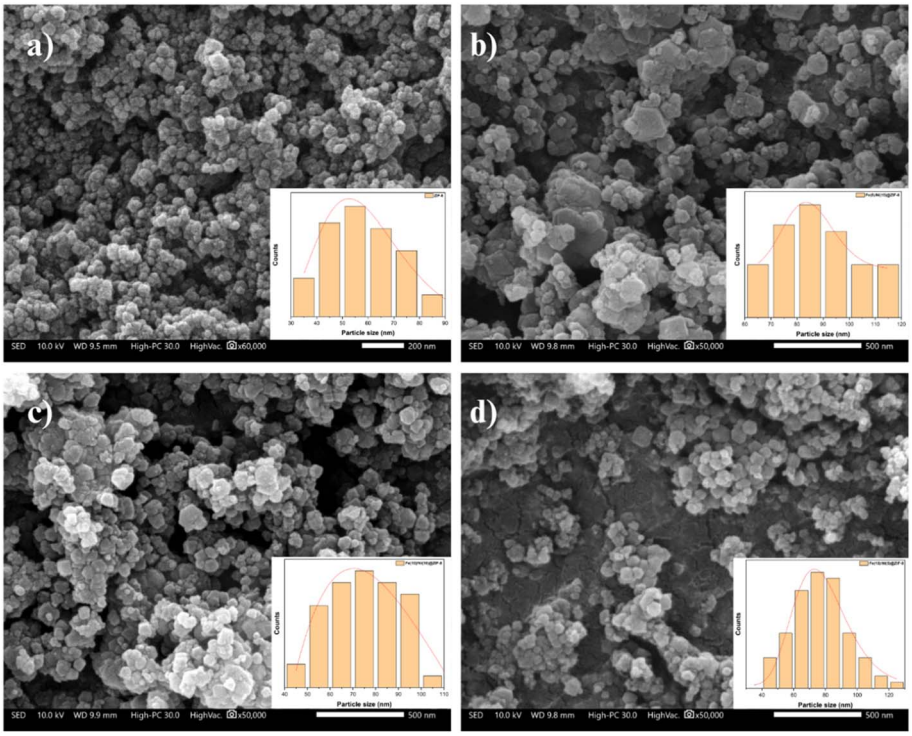

Fig. 3 FESEM image and particle size of (a) ZIF-8 (b) Fe(5)/Ni(15)@ZIF-8 (c) Fe(10)/Ni(10)@ZIF-8, and (d) Fe(15)/Ni(5)@ZIF-8.

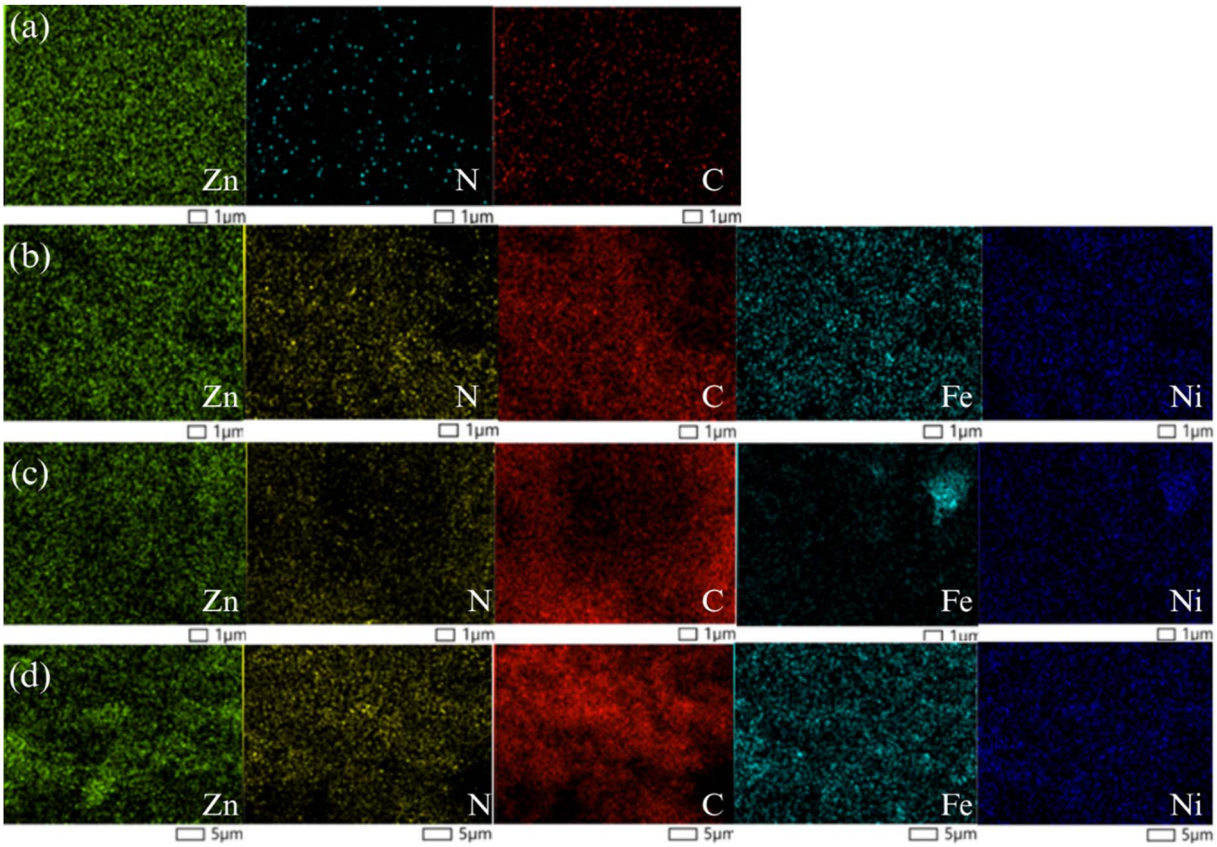

Fig. 4 EDX mapping and spectrum of (a) ZIF-8 (b) Fe(5)/Ni(15)@ZIF-8 (c) Fe(10)/Ni(10)@ZIF-8 and (d) Fe(15)/Ni(5)@ZIF-8.

Table 2 Elemental composition of Fe/Ni-doped ZIF-8 materials determined by EDX and XRF analyses

Material	Element	Mass content (%) EDX	XRF
Fe(5)/Ni(15)@ZIF-8	Zn	83.14	83.20
	Fe	5.38	4.14
	Ni	11.48	12.70
Fe(10)/Ni(10)@ZIF-8	Zn	78.34	83.70
	Fe	10.74	8.05
	Ni	10.92	8.25
Fe(15)/Ni(5)@ZIF-8	Zn	82.96	83.20
	Fe	12.50	12.40
	Ni	4.55	4.43

isotherms with type H4 hysteresis loops at high relative pressures, indicating microporous characteristics with minor contributions from secondary mesoporosity. This is consistent with previous reports showing that ZIF-8 synthesized in aqueous media at room temperature produces a type I isotherm,[29–32] confirming that the microporous structure of ZIF-8 was largely preserved after Fe and Ni incorporation.

BET analysis revealed surface area trend: Fe(10)/Ni(10)@ZIF-8 (528.08 $m^2\ g^{-1}$) > Fe(15)/Ni(5)@ZIF-8 (459.14 $m^2\ g^{-1}$) > Fe(5)/Ni(15)@ZIF-8 (445.02 $m^2\ g^{-1}$) > ZIF-8 (378.14 $m^2\ g^{-1}$). The ~40% increase in surface area for Fe(10)/Ni(10)@ZIF-8 is likely attributed to the synergistic Fe–Ni effect, which may induce structural defects, partial framework expansion, or improved nanoparticle dispersion that enhances pore accessibility. The presence of relatively high surface area is beneficial for the adsorption and photodegradation process of guest molecule such as methylene blue.

XPS. X-ray photoelectron spectroscopy (XPS) analysis was conducted to investigate the surface chemical composition and metal valence distribution in the Fe(15)/Ni(5)@ZIF-8 composite. The wide-scan survey spectrum in Fig. 5(a) reveals the presence of C, N, Zn, Fe, and Ni elements, indicating that all principal elements were successfully detected on the material surface. This confirms the successful incorporation of Fe and Ni dopants into the ZIF-8 structure while retaining Zn as the base metal. The high-resolution C 1s spectrum Fig. 5(b) displayed three characteristic peaks located at 284.7 eV, 285.7 eV, and 291.3 eV, which are assigned to C–C (sp^3), C–N bonds, and the π–π* aromatic satellite, respectively. These features are associated with the 2-methylimidazole ligand forming the ZIF-8 framework.

The N 1s spectrum Fig. 5(c) exhibited three distinct peaks at binding energies of 398.7 eV, 399.5 eV, and 407.0 eV, which correspond to N–C, N–M (where M = Zn, Fe, and Ni), and N=C bonding configurations, respectively. The presence of the N–M peak at 399.5 eV provides direct evidence that Fe and Ni successfully replaced part of the Zn sites in the ZIF-8 framework.[33,34] In Fig. 5(d), the Zn 2p spectrum showed two sharp peaks at 1021.6 eV and 1044.6 eV, attributed to Zn $2p_{3/2}$ and Zn $2p_{1/2}$, respectively. The observed spin–orbit splitting of approximately 23 eV is consistent with the expected value for Zn^{2+} species and confirms that Zn exists in a single and stable oxidation state.[35]

The Ni 2p spectrum Fig. 5(e) reveals the coexistence of Ni^{2+} and Ni^{3+} oxidation states, as evidenced by characteristic doublets at binding energies of ~853.1 eV and ~872.1 eV (Ni^{2+} $2p_{3/2}$ and $2p_{1/2}$), and ~855.1 eV and ~873.4 eV (Ni^{3+} $2p_{3/2}$ and $2p_{1/2}$). Multiple satellite peaks, especially at 859.9 eV and 880.6 eV, are attributed to Ni^{2+} shake-up transitions, suggesting strong metal–ligand interactions. Although the overall area contribution of Ni^{3+} components is slightly higher (~56.3%) than that of Ni^{2+} (~39.7%), the prominent satellite features associated with Ni^{2+} indicate its significant electronic involvement within the framework. The ~2 eV chemical shift between Ni^{2+} and Ni^{3+} confirms distinct oxidation environments. These findings suggest a complex coordination environment with dominant electronic influence from Ni^{2+} species, which may affect the redox activity and catalytic performance of the Ni-modified ZIF-8 system.[11]

The Fe 2p high-resolution spectrum Fig. 5(f) revealed multiple peaks characteristic of different oxidation states, including signals corresponding to metallic Fe, Fe^{3+} $2p_{3/2}$, mixed Fe^{3+}/Fe^{2+}, Fe^{3+} $2p_{3/2}$ satellite, Fe^{3+} $2p_{1/2}$, Fe^{2+} $2p_{1/2}$, and Fe^{3+} $2p_{1/2}$ satellite. This confirms that Fe is present in both +2 and +3 oxidation states, with Fe^{3+} being the dominant species. The prevalence of Fe^{3+} suggests a higher stability of this oxidation state within the ZIF-8 coordination environment.[36] The XPS findings confirmed the successful incorporation of Fe and Ni into the ZIF-8 framework through partial substitution of Zn. The detection of multiple oxidation states for Fe and Ni suggests the potential for improved photocatalytic performance by facilitating charge carrier mobility and introducing defect states within the material.

Structural analysis of ZIF-8 and Fe/Ni@ZIF-8 *via* GFN2-xTB computational method. Based on the experimental XRD data, supported by other characterization results, the incorporation of Fe and Ni dopants into the ZIF-8 framework has been confirmed, without inducing any phase transformation or the

Table 3 Physical properties of material

Material	S_{BET} ($m^2\ g^{-1}$)	V_p total ($cm^3\ g^{-1}$)	V_p micro ($cm^3\ g^{-1}$)	%V_p micro (%)	%V_p meso (%)
ZIF-8	378.14	0.31	0.15	48.38	51.61
Fe(5)/Ni(15)@ZIF-8	445.02	0.29	0.09	31.03	68.96
Fe(10)/Ni(10)@ZIF-8	528.08	0.36	0.11	30.55	69.44
Fe(15)/Ni(5)@ZIF-8	459.14	0.37	0.16	43.24	56.75

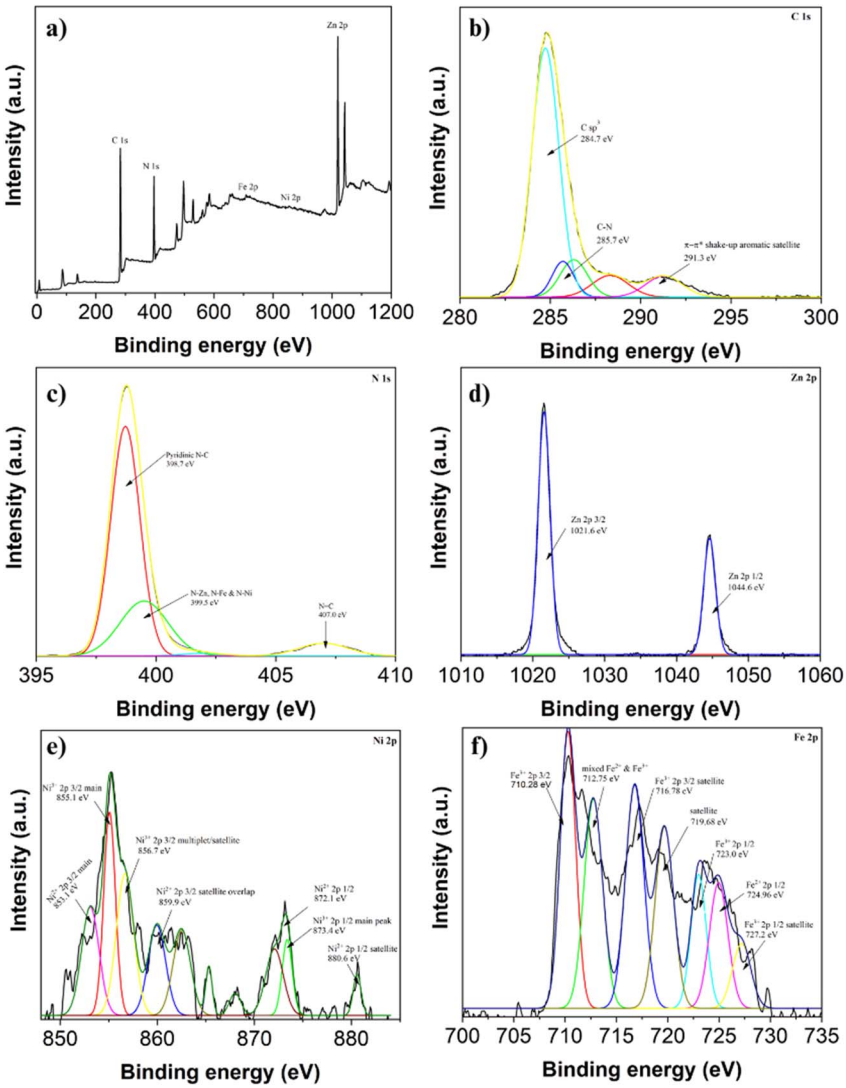

Fig. 5 XPS spectra of (a) survey spectrum, (b) C, (c) N, (d) Zn, (e) Ni, and (f) Fe.

formation of impurities. In reference to these findings, a computational study was conducted to predict the structure and energetics of partial substitution of Zn atoms by Fe and Ni within the ZIF-8 structure. The calculations were performed using the GFN2-xTB method, beginning with a model validation process against the available experimental data. This validation aimed to assess the reliability of the theoretically optimized structure, particularly in accurately representing key geometric parameters such as bond lengths and bond angles.

The optimized cluster structure model is presented in Fig. 6. Bond lengths and bond angles for the $FeNiZn_2$ cluster are listed in Table 4, while data for Zn_4, $FeZn_3$, and $NiZn_3$ clusters are provided in Table S1. The optimized geometries exhibit strong agreement with experimental structural parameters. The average relative deviation in bond lengths and angles across the four cluster models was found to be less than 5%, indicating that the optimized structures remain close to the experimental configuration. Such a low deviation supports the reliability of the GFN2-xTB method in accurately describing the fundamental structural features of the material.

The structural parameters of the Fe/Ni@ZIF-8 is summarised in Table 4. In pristine ZIF-8 structure, the characteristic Zn–N bond distance is found to be 1.99 Å which is relatively close to the reported experimentally derived structure. The presence of both Fe^{3+} and Ni^{2+} indicates distortion in M (Fe/Ni)–N bond distance to give 2.23 and 2.05 Å, respectively. This is expected since the ionic radii of Fe^{3+} is bigger than Ni^{2+} and Zn^{2+}. The distortion is predicted to alter the stability of the whole structure, especially at the supercell structure since the location of either Fe^{3+} or Ni^{2+} can be randomly distributed over the structure with many possibilities.

Binding energy calculations were carried out to assess the stability and strength of chemical interactions between metal centers and the 2-methylimidazole ligands. The geometry optimizations for each cluster were performed using the GFN2-xTB method. The results indicate that Zn^{2+}, Fe^{3+}, and Ni^{2+} ions preferentially form tetrahedral geometries, each exhibiting

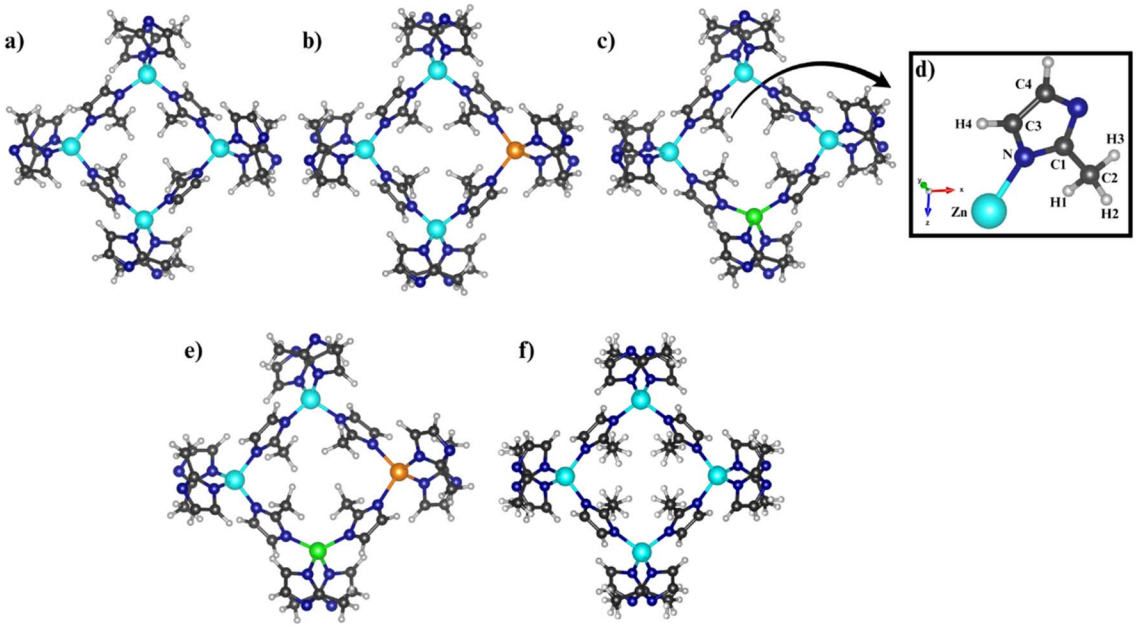

Fig. 6 The optimized geometries of (a) Zn_4–$MeIM_{12}$ (b) $FeZn_3$–$MeIM_{12}$ (c) $NiZn_3$–$MeIM_{12}$ (d) 2-metilimidazol ligand (e) $FeNiZn_2$–$MeIM_{12}$ (f) Zn_4–$MeIM_{12}$ experimental. Atom colors: zinc (cyan), iron (light brown), nickel (green), nitrogen (blue), carbon (dark gray), and hydrogen (light gray).

Table 4 Comparison of experimental and calculated bond lengths and angles of $FeNiZn_2$–MeIM12

Parameter	Type	ZIF-8_{exp}	$FeNiZn_{2calc}$	Deviation
Bond lengths (Å)	Zn–N	1.98	1.99	0.48
	Fe–N		2.23	
	Ni–N		2.05	
	C1–N1	1.33	1.33	0.36
	C3–N1	1.37	1.36	0.35
	C1–C2	1.49	1.48	0.38
	C3═C4	1.34	1.36	1.15
Average deviation				**0.54**
Bond angles (°)	N–Zn–N	109.81	107.43	2.15
	N–Fe–N		108.79	
	N–Ni–N		132.23	
	C1–N1–C3	105.30	105.31	0.01
	N1–C3–C4	108.66	108.34	0.28
	N1–C3–H4	125.70	121.36	3.44
	N1–C1–C2	123.90	123.52	0.30
	C1–C2–H1	109.50	110.40	0.82
	H1–C2–H2	109.50	107.71	1.63
Average deviation				**1.23**

a coordination number of four. The computed single-point energy output represents the total binding energy of the optimized metal–ligand complexes. The binding energies ($\Delta E_{binding}$) for Fe and Ni in the $FeZn_3$–$MeIM_{12}$, $NiZn_3$–$MeIM_{12}$, and $FeNiZn_2$–$MeIM_{12}$ clusters were calculated based on eqn (I).

$$\Delta E_{binding} = E_{complex} - (E_{Zn+2-MeIM} + E_{Fe/Ni\ metal}) \quad (I)$$

These calculated values were then used to predict the relative stability of Fe^{3+} and Ni^{2+} ions within the ZIF-8 framework, where lower binding energies indicate higher structural stability.[37] The predictive calculations were performed using the GFN2-xTB method, whose accuracy still requires validation against more rigorous approaches such as DFT. For the bimetallic cluster systems $NiZn_3$–$MeIM_{12}$ and $FeZn_3$–$MeIM_{12}$, the Fe^{3+} ion exhibited a more stable configuration with a binding energy of −18.9 eV compared to Ni^{2+}. Similarly, in the trimetallic $FeNiZn_2$–$MeIM_{12}$ system, the structure containing Fe^{3+} showed higher stability, with a binding energy 24.6 eV lower than that of the Ni^{2+}-containing structure. These results suggest that, in both bimetallic and trimetallic cluster models, Fe^{3+} is thermodynamically more stable than Ni^{2+} within the ZIF-8 framework.

Optical properties

Diffuse Reflectance UV-Visible (DR UV-Vis) spectroscopy was employed to evaluate the reduction in band gap energy (E_g) resulting from the co-doping of Fe and Ni into the ZIF-8 photocatalyst framework. The DR UV-Vis absorption spectra of pristine ZIF-8 and Fe/Ni-modified ZIF-8 in the wavelength range of 200–500 nm are presented in Fig. 7(a). The pristine ZIF-8 (black line) exhibited a sharp absorption peak at approximately 230 nm, with a rapid decline in absorbance beyond 280 nm. This behavior indicates that ZIF-8 possesses a wide band gap and is only responsive to UV radiation, in agreement with previous studies that reported a band gap of approximately 5.0 eV for ZIF-8.[18] In contrast, the introduction of transition-metal dopants notably modified the optical absorption characteristics. The single-doped Fe@ZIF-8 (purple line) showed a moderate redshift and broader absorption edge compared to pristine ZIF-8, implying partial narrowing of the band gap due to Fe-induced electronic transitions. Similarly, Ni@ZIF-8 (orange line) exhibited stronger and more extended absorption toward the visible region, indicating that Ni incorporation further enhanced light-harvesting capability.

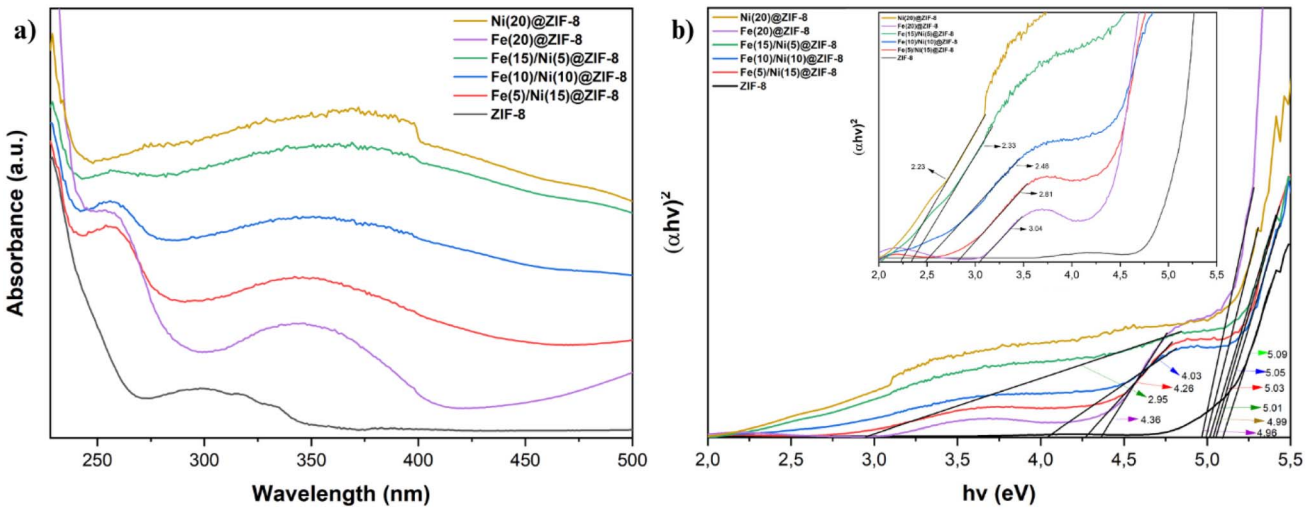

Fig. 7 (a) UV-Vis DR absorption spectra and (b) plot of *hv vs. E*.

Furthermore, co-doping with Fe and Ni produced a synergistic effect, leading to more pronounced spectral redshifts. Among the co-doped samples, Fe(15)/Ni(5)@ZIF-8 (green line) demonstrated the most significant extension of absorption into the visible light region (400–500 nm), suggesting a substantial reduction in band gap energy. Comparable but less intense redshifts were observed for Fe(10)/Ni(10)@ZIF-8 (blue line) and Fe(5)/Ni(15)@ZIF-8 (red line), indicating that the Fe/Ni ratio strongly influences the electronic structure and light absorption behavior of the materials.

Quantitative estimation of band gap energy was performed using the Tauc plot method, as described by eqn (II), where α is the absorption coefficient, h is Planck's constant, c is the speed of light, and A is a material-dependent constant. The band gap was determined by extrapolating the linear region of the plot of $(\alpha hv)^2$ *versus* photon energy (hv) to intersect the x-axis.[38] The resulting E_g values are summarized in Fig. 7(b).

$$(\alpha hv)^2 = A(hv - E_g) \quad \text{(II)}$$

Tauc plot analysis showed that the pristine ZIF-8 sample had a band gap of 5.09 eV, consistent with previously reported values ranging from 4.9 to 5.2 eV.[39] This wide band gap arises from the electronic properties of the imidazole ring in the ZIF-8 framework. The strong absorption around 230 nm corresponds to $\pi \rightarrow \pi^*$ transitions within the aromatic imidazole system, which involves excitation from the highest occupied molecular orbital (HOMO) to the lowest unoccupied molecular orbital (LUMO). Due to the large energy difference between these orbitals, this transition requires high excitation energy.[15] The introduction of transition metals, specifically the single-doped samples of Fe@ZIF-8 and Ni@ZIF-8, resulted in a noticeable reduction in band gap energy compared to pristine ZIF-8. The Fe@ZIF-8 sample exhibited band gap values of 4.96, 4.36, and 3.04 eV, while Ni@ZIF-8 showed band gaps of 4.99 and 2.23 eV, depending on the transition edge analysed. These results indicate that the incorporation of either Fe or Ni individually can effectively narrow the band gap and enhance visible-light absorption. The Fe(15)/Ni(5)@ZIF-8 sample exhibited band gap values of 5.01, 2.95, and 2.33 eV, depending on the absorption edge analysed. These values are comparable to those previously reported for Fe-ZIF-8 materials, which exhibited band gaps ranging from 2.1 to 3.1 eV depending on dopant concentration.[15] Similarly, the Fe(10)/Ni(10)@ZIF-8 and Fe(5)/Ni(15)@ZIF-8 samples showed band gap values of 5.05, 4.03, and 2.48 eV; and 5.03, 4.26, and 2.81 eV, respectively. These findings are consistent with reported band gaps for Ni-ZIF-8, ranging from 3.05 to 5.02 eV, also influenced by doping concentration.[11]

The observed reduction in band gap energy upon Fe and Ni co-doping can be explained by the incorporation of Fe^{2+}/Fe^{3+} and Ni^{2+} ions into the ZIF-8 lattice, which introduces new energy levels within the band structure through partially filled d-orbitals.[40] These transition metal ions create additional electronic states that act as intermediate energy levels between the valence and conduction bands, thereby facilitating lower-energy electronic transitions.[31] The formation of these intermediate states effectively narrows the band gap and introduces a new Fermi level, which disturbs the original band structure. Moreover, the appearance of absorption bands in the visible region is attributed to metal-to-metal charge transfer (MMCT) transitions, particularly from and Fe^{2+}/Fe^{3+} and Ni^{2+} to Zn^{2+}, enabled by the newly formed Fermi level acting as an alternative energy pathway.[41] Overall, the significant narrowing of band gap energy in the Fe/Ni-doped ZIF-8 materials suggests enhanced photocatalytic potential under visible light irradiation.

Photocatalytic activity

(a) Influence of light exposure duration on methylene blue photodegradation. The effect of irradiation time was investigated to determine the optimum exposure duration required for the photodegradation of methylene blue (MB) using pristine ZIF-8, single doped (Fe@ZIF-8 or Ni@ZIF-8), and co-doped Fe/Ni@ZIF-8 photocatalysts under visible light. Prior to irradiation, adsorption–desorption equilibrium was ensured for all

samples through dark-condition testing Fig. 8. Both pristine ZIF-8 and its composites exhibit high porosity and superior adsorption capacity compared to conventional metal oxides. A notable increase in MB removal was observed during the first 15–45 minutes of contact, with equilibrium reached after 60 minutes, where approximately 30% of MB was adsorbed. Interestingly, the single-doped Fe@ZIF-8 and Ni@ZIF-8 exhibited lower adsorption capacity than pristine ZIF-8, which is consistent with previous findings[11,29] showing that single metal doping tends to reduce the specific surface area due to partial pore blockage by metal species.[41] In contrast, the co-doped Fe/Ni@ZIF-8 displayed higher adsorption performance, in line with its increased S_{BET} value compared to pristine ZIF-8, suggesting that the synergistic effect between Fe and Ni enhances surface accessibility and facilitates stronger dye–surface interactions. Various interactions such as π–π stacking, hydrogen bonding, electrostatic attraction, and pore filling were responsible for the adsorption behavior.[21,29]

Fig. 9(a) demonstrates the photodegradation performance under visible light. In the absence of photocatalyst, MB degradation was negligible, confirming the necessity of catalytic assistance to break the dye's complex molecular bonds.[42,43] All co-doped photocatalysts displayed improved performance over pristine ZIF-8 and single doped (Fe@ZIF-8 and Ni@ZIF-8), with Fe(15)/Ni(5)@ZIF-8 achieving the highest efficiency of 83.51% after 60 minutes of visible-light irradiation. The superior activity of this sample is attributed to its narrower band gap Fig. 7(b), which facilitates charge separation, as well as an optimal Fe/Ni ratio that effectively promotes the formation of mid-gap energy levels, enhancing photocatalytic charge transfer.[40]

The enhanced performance is driven by a synergistic effect between the bimetallic nodes within the ZIF-8 framework, enabling efficient metal-to-metal charge transfer (MMCT) among Fe^{3+}, Ni^{2+}, and Zn^{2+} ions.[44] In contrast, the single-doped Fe@ZIF-8 and Ni@ZIF-8 showed poorer performance than the co-doped samples, likely due to the absence of Fe–Ni synergistic interactions that facilitate charge transfer and suppress electron–hole recombination. However, lower degradation efficiency observed in Fe(10)/Ni(10)@ZIF-8 and Fe(5)/Ni(15)@ZIF-8 is likely due to excessive dopant content that surpasses the optimum level needed to maintain charge carrier separation and structural stability. This excess may induce defect states or recombination centers that hinder photocatalytic efficiency. It also suggests that the balance between dopant amount and dispersion must be carefully controlled, as high-energy surfaces in MOFs are prone to particle aggregation and framework distortion under high dopant loads.[11,45] Therefore, further optimization of Fe/Ni ratios is essential to maximize the synergistic effect without compromising the MOF integrity or introducing electronic trap states.

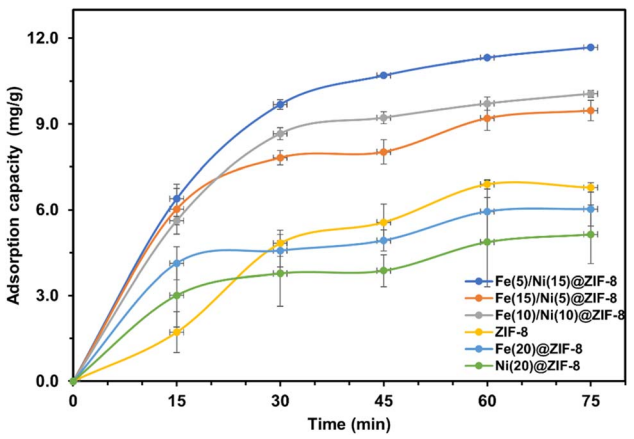

Fig. 8 Adsorption capacity of ZIF-8, Fe@ZIF-8, Ni@ZIF-8, and Fe/Ni@ZIF-8 composites.

The degradation kinetics of MB using pristine ZIF-8, single doped, and Fe/Ni co-doped composites were evaluated using a pseudo-first-order kinetic model Fig. 9(b). The results demonstrated good linearity with R^2 values approaching unity for all samples, confirming that the degradation followed pseudo-first-order kinetics. Among the materials tested, Fe(15)/Ni(5)@ZIF-8 exhibited the highest degradation rate constant of 2.73×10^{-2} min^{-1}. This finding validates that optimizing the Fe/Ni dopant ratio can significantly enhance photocatalytic performance. The kinetic modeling further supports that the degradation rate is governed by the intrinsic photocatalytic activity of the materials—primarily charge transfer dynamics—rather than mass diffusion limitations. Therefore, the improvement in performance of Fe/Ni@ZIF-8 composites is attributed to enhanced charge separation and electron transfer efficiency.[15]

(b) Effect of solution pH on the photocatalytic degradation of methylene blue. The effect of pH on the photocatalytic performance of Fe(15)/Ni(5)@ZIF-8 was further explored by varying the initial solution pH at values of 3, 5, 7, 9, and 11, adjusted using HCl or NaOH as shown on Fig. 10. The results demonstrate that pH has a significant influence on photocatalytic degradation efficiency. The lowest performance was observed under strongly acidic conditions at pH 3 (~91%), indicating that excess proton concentration is unfavorable. In near-neutral conditions (pH 5–7), the efficiency improved to ~92%, while basic environments yielded the best performance, with degradation efficiencies of 94% (pH 9) and 96.86% (pH 11). Despite these variations, the relatively narrow efficiency range (91–96%) highlights the chemical robustness and stability of the Fe/Ni@ZIF-8 composite across a broad pH spectrum.[13,46]

This pH dependence is primarily attributed to the electrostatic interactions between MB molecules and the surface of the photocatalyst. In acidic media, elevated H^+ concentrations compete with positively charged MB molecules for adsorption sites, reducing adsorption efficiency and thus suppressing photocatalytic performance.[47] Conversely, under alkaline conditions, the presence of OH^- ions enhance electrostatic attraction with MB and contributes to the generation of highly reactive hydroxyl radicals (·OH), which play a critical role in the oxidative degradation pathway.[48] Therefore, the enhanced activity under basic conditions can be associated with both favorable adsorption interactions and increased radical formation.

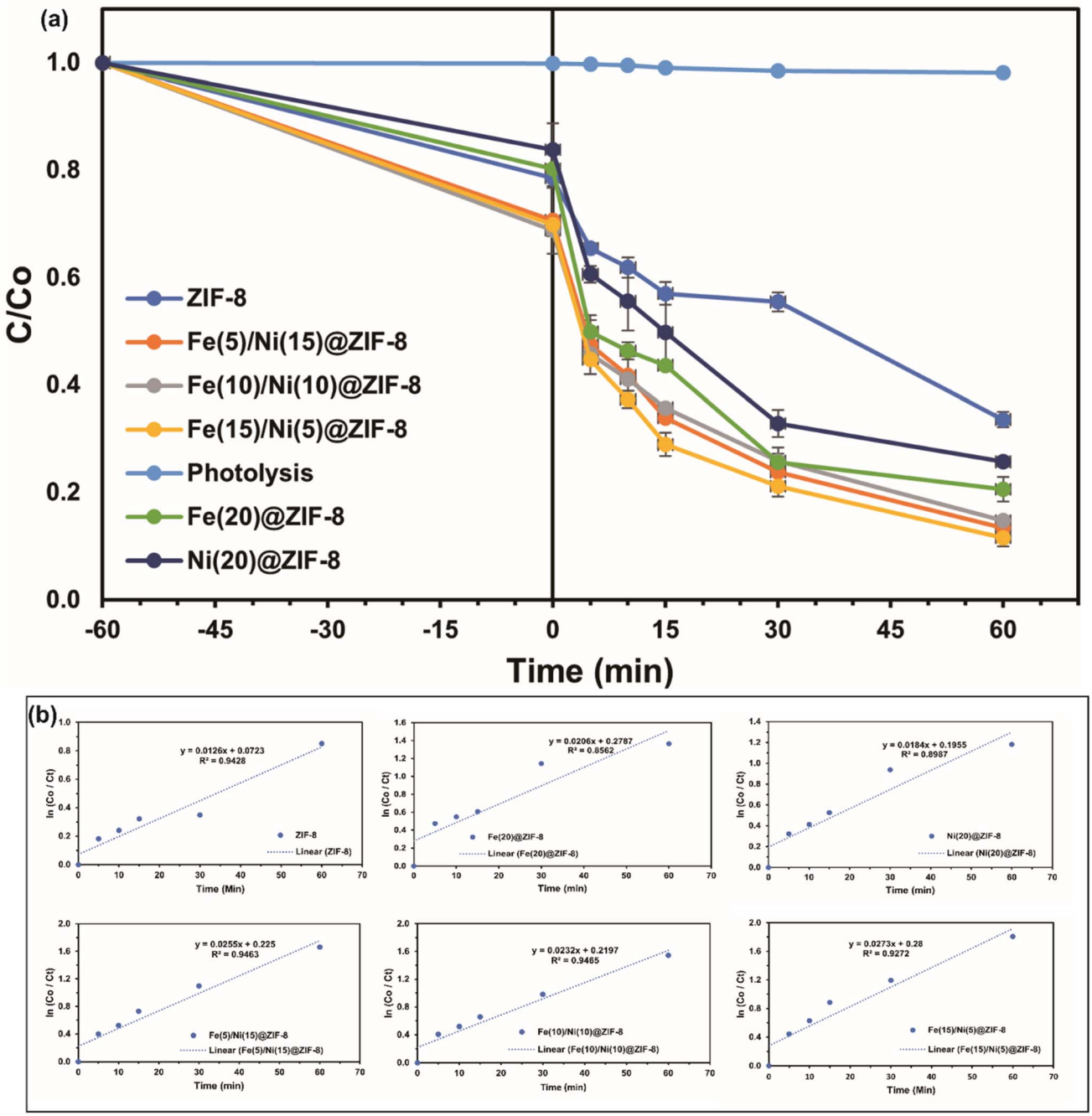

Fig. 9 (a) Effect of irradiation of visible light on the degradation of MB (b) pseudo first order kinetic plot ($W = 10$ mg, $V = 10$ mL, $C = 30$ mg L^{-1}, pH = 6.8, dark = 60 min, vis light = 60 min).

(c) Effect of photocatalyst dosage on the photodegradation of methylene blue dye. The amount of photocatalyst used plays a critical role in determining the overall degradation efficiency of methylene blue (MB), as it directly affects the number of available active sites responsible for generating reactive species. In this study, the influence of catalyst dosage was investigated by varying the amount of Fe(15)/Ni(5)@ZIF-8 photocatalyst at 2 mg, 3 mg, 5 mg, 10 mg, and 15 mg dispersed in 10 mL of MB solution (30 mg L^{-1}). The corresponding photocatalytic performance is presented in Fig. 11.

A substantial increase in MB degradation efficiency was observed as the catalyst dosage was raised from 2 to 10 mg. At lower dosages (2–5 mg), the limited number of surface-active sites hinders the effective formation of reactive oxygen species (ROS), leading to lower degradation efficiency. As the dosage increased to 10 mg, a marked enhancement was observed due to the increased number of active sites, greater light absorption, and improved MB adsorption on the catalyst surface. However, further increasing the dosage to 15 mg resulted in a slight decrease in degradation efficiency. This may be attributed to

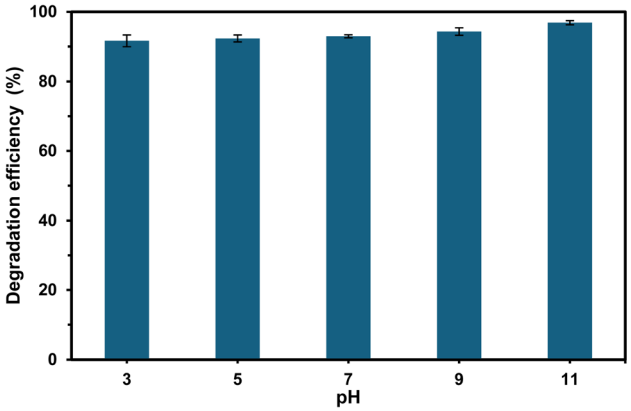

Fig. 10 Photocatalytic activity of Fe(15)/Ni(5)@ZIF-8 at various pH (W = 10 mg, V = 10 mL, C = 30 mg L^{-1}, vis light = 180 min).

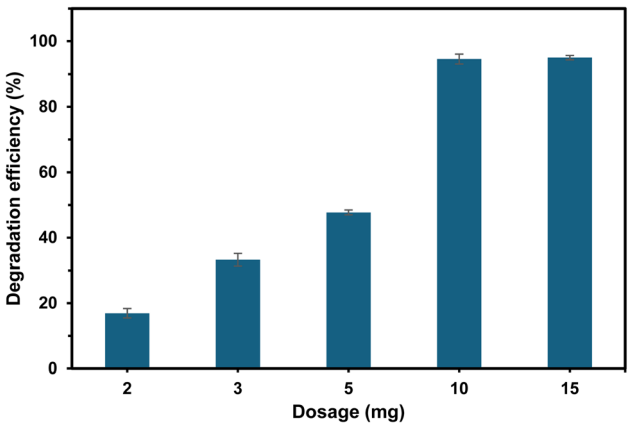

Fig. 11 Photocatalytic activity of Fe(15)/Ni(5)@ZIF-8 at various dosage (C_0 = 30 mg L^{-1}, V = 10 mL, pH = 11, vis light = 180 min).

particle agglomeration and light shielding effects, which reduce light penetration and photon utilization. Moreover, the excess amount of catalyst may lead to increased charge carrier recombination due to overlapping surface areas.[49] Based on these observations, 10 mg was identified as the optimal dosage, achieving the highest degradation efficiency of 94.57% for 10 mL of MB solution (30 mg L^{-1}) under visible light irradiation. These results underscore the importance of optimizing photocatalyst mass to achieve a balance between active site availability and light-harvesting efficiency.

(d) Effect of initial dye concentration on the photodegradation of methylene blue. The initial concentration of methylene blue (MB) plays a crucial role in determining the photocatalytic performance of Fe(15)/Ni(5)@ZIF-8. The influence of varying MB concentrations on degradation efficiency was assessed at 15, 30, 45, and 60 mg L^{-1}, and the results are illustrated in Fig. 12. As shown in the figure, all MB concentrations exhibit a relatively steady decline during the dark adsorption phase (−60 to 0 minutes), indicating that adsorption–desorption equilibrium was successfully established prior to light irradiation. This equilibrium ensures that the observed photocatalytic activity is not influenced by additional adsorption effects during the irradiation process.

At the lowest tested concentration (15 mg L^{-1}), the photocatalyst demonstrated a high degradation efficiency of approximately 93% after 180 minutes of irradiation. Increasing the MB concentration to 30 mg L^{-1} resulted in the highest degradation efficiency, reaching 95.06%, with a final C/C_0 value of approximately 0.029. However, further increases in initial concentration to 45 mg L^{-1} and 60 mg L^{-1} led to a marked decrease in degradation efficiency, yielding final values of 85.3% and 82%, respectively. This decline in performance is primarily attributed to limited light penetration caused by the higher optical density of the solution, which reduces photon–catalyst interactions. Additionally, the increased number of MB molecules may exceed the available active sites, thereby restricting the extent of photocatalytic reactions.[50] Taken together, these results suggest that a starting concentration of 30 mg L^{-1} offers optimal conditions for efficient photocatalytic degradation. This concentration maintains a favorable balance between dye molecules and active catalytic sites, supporting effective photon utilization and charge separation dynamics within the photocatalytic system.[10,11]

Following the determination of optimal conditions for MB degradation—including irradiation time, catalyst dosage, solution pH, and initial dye concentration—a comparative analysis was conducted to assess the relative performance of the Fe(15)Ni(5)@ZIF-8 photocatalyst. Table 5 summarizes previously reported ZIF-8-based photocatalysts, highlighting differences in reaction conditions and degradation efficiencies.

While differences in testing parameters such as photocatalyst dosage, dye concentration, and irradiation time limit direct comparison, the Fe/Ni@ZIF-8 photocatalyst exhibited excellent activity, achieving 96.05% methylene blue degradation within 180 min under visible light, even at a high dye concentration (30 mg L^{-1}), indicating strong stability toward higher pollutant loads. The superior performance is mainly attributed to the Fe–Ni synergistic effect, which enhances charge separation and electron transfer efficiency. Moreover, the simple room-temperature, water-based synthesis demonstrates an energy-efficient and environmentally friendly approach. These findings highlight that Fe/Ni@ZIF-8 combines high photocatalytic performance with sustainable synthesis, making it a promising candidate for practical wastewater treatment.

(e) Identification of reactive species involved in photocatalytic MB degradation. To elucidate the role of reactive species in the photocatalytic degradation mechanism, scavenger experiments were conducted, and the results are presented in Fig. 13. The control experiment, performed without any scavengers, yielded the highest degradation efficiency of 95.37%, which served as the benchmark for evaluating the contribution of each reactive species.

Upon the addition of isopropanol (IPA), a known hydroxyl radical (·OH) scavenger, the degradation efficiency decreased significantly to 81%. This observation highlights ·OH as the predominant active species responsible for MB degradation. Similarly, the presence of ethylenediaminetetraacetic acid (EDTA), a hole (h^+) scavenger, resulted in a reduction in efficiency to 82.77%, confirming the substantial contribution of photogenerated holes as secondary active species. In contrast, the addition of ascorbic acid, which selectively scavenges superoxide radicals

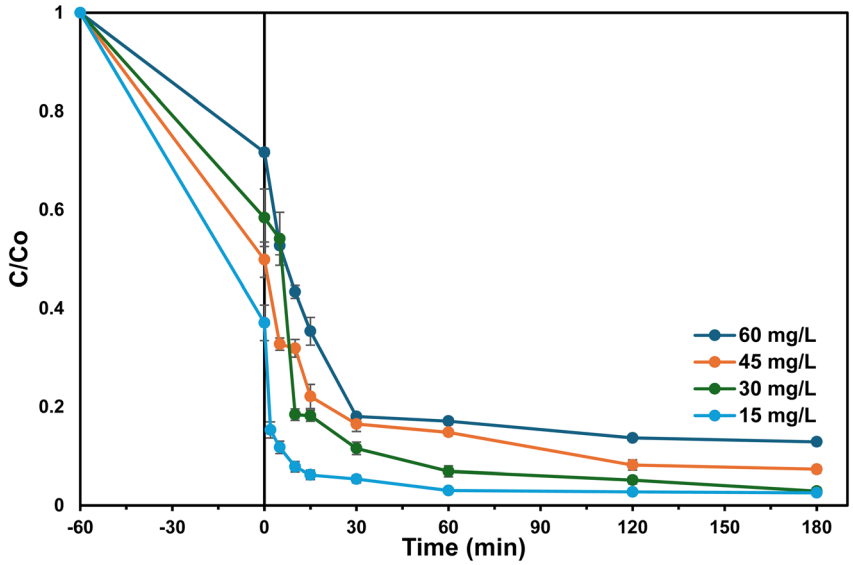

Fig. 12 Photocatalytic activity of Fe(15)/Ni(5)@ZIF-8 at various initial dye concentration on MB degradation ($W = 10$ mg, $V = 10$ mL, pH = 11, dark = 60 min, vis light = 180 min).

($\cdot O_2^-$), led to only a slight reduction in degradation efficiency (92.19%), indicating a relatively minor role of $\cdot O_2^-$ in the overall degradation process.

These findings suggest that the photocatalytic mechanism primarily follows a dual-pathway route in which hydroxyl radicals act as the dominant oxidizing agents, while holes serve a complementary function. The correlation between h^+ and $\cdot OH$ is further supported by the observation that inhibition of hole formation in the valence band (VB) directly affects the generation of $\cdot OH$, thereby diminishing photocatalytic performance. This mechanism aligns with previous reports identifying $\cdot OH$ as the principal reactive species in MB degradation over ZIF-8-based photocatalysts.[54,55]

(f) Stability and reusability of the photocatalysts. The stability and reusability of the Fe/Ni@ZIF-8 photocatalyst were evaluated through three consecutive photodegradation cycles under visible-light irradiation (Fig. 14). The degradation efficiency gradually declined from approximately 91% in the first cycle to around 72% and 47% in the second and third cycles, respectively. This decrease is primarily attributed to partial catalyst loss during repetitive washing and drying processes.[56] To assess the structural stability of the material during the photocatalytic process, atomic absorption spectroscopy (AAS) was employed to detect possible metal leaching into the solution. The results (Table S2) revealed that Fe was not detected in the filtrate, whereas measurable concentrations of Ni and Zn were observed after the degradation process. This indicates partial leaching of Ni and Zn ions from the ZIF-8 framework into the aqueous phase.[57] Zn leaching suggests minor framework degradation under light exposure, while Ni leaching is likely associated with the detachment of surface-active sites during the reaction. Despite the decline in degradation efficiency and partial metal leaching, the Fe/Ni@ZIF-8 composite maintained reasonable structural and functional stability after multiple cycles. These findings demonstrate that Fe/Ni@ZIF-8 possesses promising reusability under visible light; however, further optimization is required to enhance framework robustness and minimize metal leaching for long-term environmental applications. With its combination of high photocatalytic performance, adequate stability, and environmentally benign synthesis route, Fe/Ni@ZIF-8 presents itself as a potential candidate for scalable and sustainable water treatment systems.

(g) Proposed mechanism for methylene blue degradation over Fe/Ni@ZIF-8 photocatalyst. The photodegradation of methylene blue (MB) by Fe/Ni@ZIF-8 proceeds *via* a two-step process: initial adsorption under dark conditions, followed by visible-light-induced photocatalysis (Fig. 15). In the dark phase, MB molecules are adsorbed onto the active sites of Fe/Ni@ZIF-8 through physical and chemical interactions, leading to a pre-

Table 5 Comparative study of ZIF-8-based photocatalyst

Photocatalyst	Reaction condition	Degradation efficiency (%)	Reference
ZIF-8	25 mg; 50 mL; MB 10 mg L^{-1}; 120 min; UV light	82	51
ZIF-8@TiO_2	10 mg; 20 mL; MB 1.6 mg L^{-1}; 120 min; UV light	87.50	52
Ni(20)-ZIF-8	30 mg; 50 mL; MB 30 mg L^{-1}; 150 min; 365 UV light	93.22	11
Fe-ZIF-8	10 mg; 500 mL; 30 mg L^{-1}; 300 min; visible light	90	15
Fe@ZIF-8	10 mg; 25 mL; MB 10 mg L^{-1}; 55 min; visible light	99	53
Ni@ZIF-8	10 mg; 25 mL; MB 10 mg L^{-1}; 55 min; visible light	95	53
Fe(15)/Ni(5)@ZIF-8	30 mg; 10 mL; MB 30 mg L^{-1}; 180 min; visible light	95.06	This work

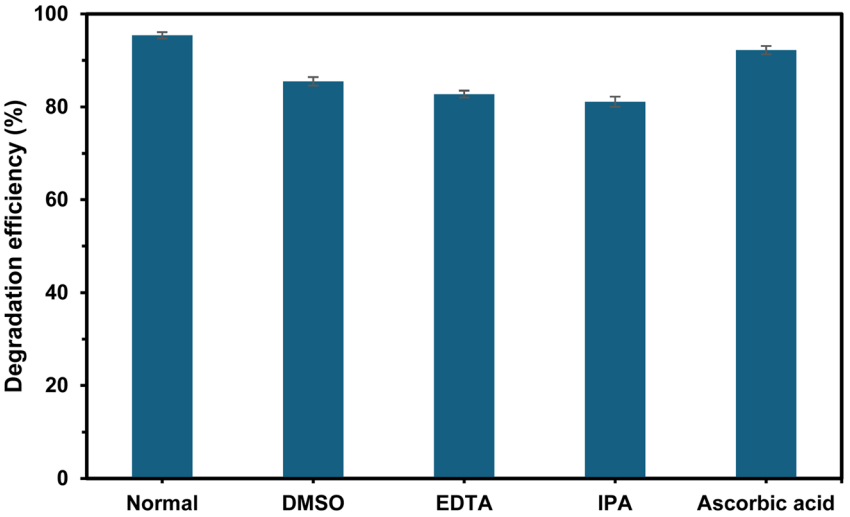

Fig. 13 Trapping experiment ($W = 10$ mg, $V = 10$ mL, $C = 30$ mg L^{-1}).

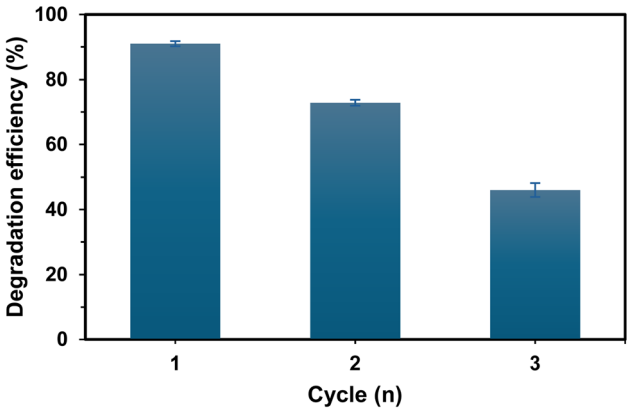

Fig. 14 Reusability of Fe/Ni@ZIF-8 photocatalyst under visible light.

concentrated state that enhances the interaction probability with incident photons during illumination.[11,21]

Upon visible light irradiation, excitation occurs *via* a ligand-to-metal charge transfer (LMCT) process from the 2-methylimidazole ligands to the metal clusters, generating electron–hole (e^-/h^+) pairs.[58] The photogenerated holes (h^+) oxidize H_2O to hydroxyl radicals ($\cdot OH$), while the excited electrons (e^-) reduce dissolved O_2 to superoxide radicals ($\cdot O_2^-$).[59] The introduction of Fe and Ni dopants into the ZIF-8 framework promotes the formation of Schottky barriers and new energy levels, which effectively suppress e^-/h^+ recombination.[60]

Furthermore, the system enables efficient metal-to-metal charge transfer (MMCT) among Fe–N, Ni–N, and Zn–N centers, facilitating prolonged charge separation and enhanced photocatalytic activity.[22] These reactive oxygen species (ROS), primarily $\cdot OH$ and $\cdot O_2^-$, subsequently attack the MB molecules, breaking them down into simpler intermediates that are likely more environmentally benign, as summarized in the following reaction sequence:

(1) Adsorption phase

$$\text{Fe/Ni@ZIF-8} + \text{MB}_{(aq)} \rightarrow \text{MB}_{(ads)}$$

(2) Photoexcitation (LMCT)

$$h\nu + \text{Fe/Ni@ZIF-8} \rightarrow e_{(CB)}^- + h_{(VB)}^+$$

(3) Charge migration (MMCT)

$$\text{Fe–N } (e^-) \rightarrow \text{Ni–N } (e^-) \rightarrow \text{Zn–N } (e^-)$$

(4) ROS generation

$$e^- + O_2 \rightarrow \cdot O_2^-$$

$$h_{(VB)}^+ + H_2O \rightarrow \cdot OH + H^+$$

(5) ROS-mediated degradation

$$\text{MB} + \cdot OH \rightarrow \text{MB intermediate}$$

$$\text{MB} + \cdot O_2^- \rightarrow \text{MB intermediate}$$

$$\text{MB} + h^+ \rightarrow \text{MB intermediate}$$

$$\text{MB} + e^- \rightarrow \text{MB intermediate}$$

(6) Charge recombination (non-productive)

$$e_{(CB)}^- + h_{(VB)}^+ \rightarrow \text{heat} \quad \text{(III)}$$

This mechanism highlights the synergistic effect of dual-metal doping and interfacial charge dynamics, which collectively enhance photocatalytic degradation efficiency.

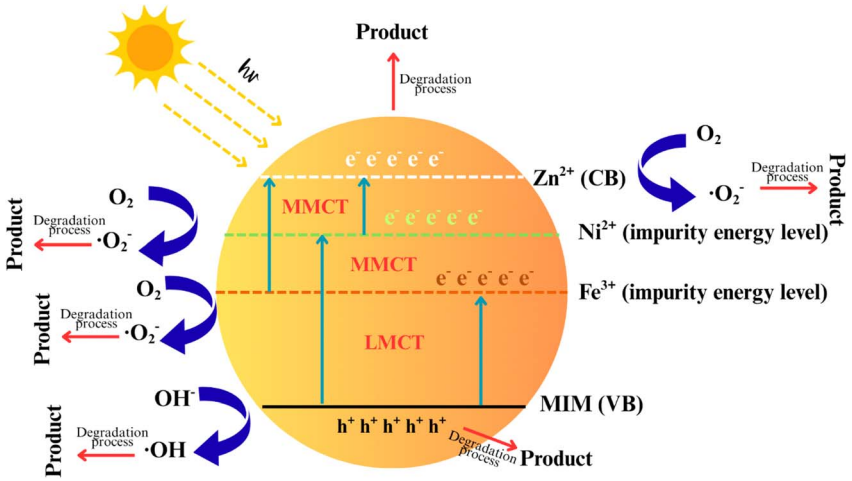

Fig. 15 Proposed diagram of charge migration pathway through LMCT and MMCT on MB degradation mechanism using Fe(15)/Ni(5)@ZIF-8.

Conclusion

This study successfully demonstrated the synthesis of a highly efficient bimetallic Fe/Ni@ZIF-8 photocatalyst through a simple, environmentally friendly, one-pot synthesis at room temperature. The novel co-doping strategy significantly narrows the band gap of ZIF-8, enhancing its visible light absorption and photocatalytic activity. The optimized Fe(15)/Ni(5)@ZIF-8 catalyst achieved the highest photodegradation efficiency of 95.06% for 30 mg L^{-1} methylene blue solution under visible light irradiation (180 min, 10 mg catalyst, pH 11), with a reaction rate constant of 2.73 × 10^{-2} min^{-1}. The core innovation of this work lies in harnessing the Fe/Ni bimetallic synergistic effect, which effectively promotes electron–hole pair separation and boosts the generation of reactive oxygen species. This study not only presents a promising, high-performance catalyst for treating dye-polluted wastewater but also offers a facile and green modification strategy for designing advanced MOF-based materials for environmental applications.

Author contributions

Siti Saenab: writing – original draft, methodology, investigation, formal analysis, data curation. Oka Pradipta Arjasa: data curation, investigation, writing – review. Dwi Siswanta: writing – review & editing, supervision, resources, project administration, methodology, data curation, visualization. Fajar Inggit Pambudi: writing – review & editing, supervision, resources, project administration, methodology, data curation, visualization.

Conflicts of interest

The authors declare that they have no known competing financial interests or personal relationships that could have appeared to influence the work reported in this paper.

Data availability

The data supporting this article have been included as part of the supplementary information (SI). Supplementary information: contains a coloured image of the samples, the XRD pattern, the N_2 adsorption-desorption isotherm, structural parameters from the GFN2-xTB calculations, and the detailed leaching data. See DOI: https://doi.org/10.1039/d5ra05662d.

Acknowledgements

The authors acknowledge the Analytical and Environmental Laboratory, Department of Chemistry, Universitas Gadjah Mada Yogyakarta, Indonesia, for facilities supporting this work.

References

1 N. M. Mahmoodi and J. Abdi, *Microchem. J.*, 2019, **144**, 436–442.
2 L. Pereira and M. Alves, in *Environmental Protection Strategies for Sustainable Development*, Springer Netherlands, 2012, pp. 111–162.
3 X. Wang, H. Li, Y. Song, Y. Shi, J. Fan and L. Cheng, *Polyhedron*, 2024, **255**, 117130.
4 M. A. Ahmed, Z. M. Abou-Gamra, H. A. A. Medien and M. A. Hamza, *J. Photochem. Photobiol., B*, 2017, **176**, 25–35.
5 H. He, W. Peng, J. Jiang, X. Xia, J. Luo, S. Luo, X. Wang, K. Yang and C. Yu, *Colloids Surf., A*, 2025, **723**, 137420.
6 H. He, Z. Luo and C. Yu, *Colloids Surf., A*, 2021, **613**, 126099.
7 S. Xie, J. Jiang, G. Zhou, Y. Chen, A. Zhang, X. Xia, M. Shi, B. Deng, C. Yu and H. He, *Inorg. Chem. Commun.*, 2025, **173**, 113845.
8 Z. Youssef, L. Colombeau, N. Yesmurzayeva, F. Baros, R. Vanderesse, T. Hamieh, J. Toufaily, C. Frochot, T. Roques-Carmes and S. Acherar, *Dyes Pigm.*, 2018, **159**, 49–71.
9 C. Han, X. Zhang, S. Huang, Y. Hu, Z. Yang, T. Li, Q. Li and J. Qian, *Adv. Sci.*, 2023, **10**(19), 2300797.
10 R. Ediati, L. L. Zulfa, I. Maulidah, D. O. Sulistiono, H. Fansuri, A. Rosyidah, F. Martak, D. Hartanto, M. A. B. Abdullah, W. P. Utomo, E. N. Kusumawati and M. Shirai, *S. Afr. J. Chem. Eng.*, 2023, **46**, 132–142.
11 L. L. Zulfa, A. R. P. Hidayat, W. P. Utomo, R. Subagyo, E. N. Kusumawati, Y. Kusumawati, D. Hartanto,

W. Widyastuti and R. Ediati, *Case Stud. Chem. Environ. Eng.*, 2024, **10**, 100828.
12 M. Zhu, S. Darbha, B. Seemala and P. Ratnasamy, *Catal. Commun.*, 2013, **32**, 36–40.
13 X. Zhang and J. Jiang, *J. Phys. Chem. C*, 2013, **117**, 18441–18447.
14 F. Cacho-Bailo, B. Seoane, C. Téllez and J. Coronas, *J. Membr. Sci.*, 2014, **464**, 119–126.
15 M. T. Thanh, T. V. Thien, P. D. Du, N. P. Hung and D. Q. Khieu, *J. Porous Mater.*, 2018, **25**, 857–869.
16 X. Zhang, Z. Zhao, S. Zhao, S. Xiang, W. Gao, L. Wang, J. Xu and Y. Wang, *J. Catal.*, 2022, **415**, 218–235.
17 J. Abdi, *Colloids Surf., A*, 2020, **604**, 125330.
18 L. E. Mphuthi, E. Erasmus and E. H. G. Langner, *ACS Omega*, 2021, **6**, 31632–31645.
19 L. Li, Z. Bin Fang, W. Deng, J. D. Yi, R. Wang and T. F. Liu, *CCS Chem.*, 2022, **4**, 2782–2792.
20 J. Tan, H. Ren, Z. Zhao, X. Xin, Y. Shi, D. Yang and Z. Jiang, *Chem. Eng. J.*, 2023, **466**, 143259.
21 A. R. P. Hidayat, D. O. Sulistiono, I. K. Murwani, B. F. Endrawati, H. Fansuri, L. L. Zulfa and R. Ediati, *J. Environ. Chem. Eng.*, 2021, **9**, 106675.
22 B. Yao, S.-K. Lua, H.-S. Lim, Q. Zhang, X. Cui, T. J. White, V. P. Ting and Z. Dong, *Microporous Mesoporous Mater.*, 2021, **314**, 110777.
23 K. S. Park, Z. Ni, A. P. Côté, J. Y. Choi, R. Huang, F. J. Uribe-Romo, H. K. Chae, M. O'Keeffe and O. M. Yaghi, Exceptionalchemical and thermal stability of zeolitic imidazolate frameworks, *Proc. Natl. Acad. Sci. U. S. A.*, **103**(27), 10186–10191.
24 A. M. G. Muchlis and C. C. Lin, *J. Mater. Chem. A*, 2024, **12**, 26471–26483.
25 E. Santoso, R. Ediati, Z. Istiqomah, D. O. Sulistiono, R. E. Nugraha, Y. Kusumawati, H. Bahruji and D. Prasetyoko, *Microporous Mesoporous Mater.*, 2021, **310**, 110620.
26 B. Yang, J. Li, L. Zhang and G. Xu, *Analyst*, 2016, **141**, 5822–5828.
27 X. Wang, H. Wang, J. Cheng, H. Li, X. Wu, D. Zhang, X. Shi, J. Zhang, N. Han and Y. Chen, *Chem. Eng. J.*, 2023, **466**, 143201.
28 Y. Shi, J. Huang, L. Chen, S. Wang, J. Xu, F. Zhu, S. Cui, J. Zheng and G. Ouyang, *J. Porous Mater.*, 2022, **424**, 127465.
29 L. L. Zulfa, R. Ediati, A. R. P. Hidayat, R. Subagyo, N. Faaizatunnisa, Y. Kusumawati, D. Hartanto, N. Widiastuti, W. P. Utomo and M. Santoso, *RSC Adv.*, 2023, **13**, 3818–3834.
30 S. Eslava, L. Zhang, S. Esconjauregui, J. Yang, K. Vanstreels, M. R. Baklanov and E. Saiz, *Chem. Mater.*, 2013, **25**, 27–33.
31 J. Madhavan, P. S. S. Kumar, S. Anandan, M. Zhou, F. Grieser and M. Ashokkumar, *Chemosphere*, 2010, **80**, 747–752.
32 S. Ning, Y. Su, W. Deng and B. Zhao, *Sep. Purif. Technol.*, 2024, **335**, 126207.
33 B. Shen, B. Wang, L. Zhu and L. Jiang, *Nanomaterials*, 2020, **10**, 1636.
34 H. Gong, X. Zheng, K. Zeng, B. Yang, X. Liang, L. Li, Y. Tao and R. Yang, *Carbon*, 2021, **174**, 475–483.
35 Y.-C. Liang and C.-C. Wang, *RSC Adv.*, 2018, **8**, 5063–5070.
36 U. Imtiaz, N. Iqbal, T. Noor, M. Z. Amjad, M. Raza and M. Asad Ali, *Int. J. Hydrogen Energy*, 2022, **47**, 37002–37012.
37 A. N. Mallya and S. Panda, *Comput. Theor. Chem.*, 2021, **1202**, 113288.
38 D. Roy, A. K. Yadav, K. B. Singh and G. Pandey, *Jordan J. Phys.*, 2023, **16**, 181–194.
39 F. Wang, Z. Liu, H. Yang, Y. Tan and J. Zhang, *Angew. Chem., Int. Ed.*, 2011, **50**, 450–453.
40 D. Han, Y. Han, J. Li, X. Liu, K. W. K. Yeung, Y. Zheng, Z. Cui, X. Yang, Y. Liang, Z. Li, S. Zhu, X. Yuan, X. Feng, C. Yang and S. Wu, *Appl. Catal., B*, 2020, **261**, 118248.
41 S. Wang, F. Meng, X. Sun, M. Bao, J. Ren, S. Yu, Z. Zhang, J. Ke and L. Zeng, *Appl. Surf. Sci.*, 2020, **528**, 147053.
42 T. Kamatchi, P. Kumaresan and G. Suresh, *J. Mater. Sci.: Mater. Electron.*, 2024, **35**, 213.
43 Z. W. Zena, D. M. Andoshe, L. T. Tufa, A. B. Gemta and F. B. Dejene, *Phys. Scr.*, 2024, **99**, 045934.
44 R. Li, T. Chen, J. Lu, H. Hu, H. Zheng, P. Zhu and X. Pan, *Water Res.*, 2023, **229**, 119366.
45 M. Rahman, M. Lutfor Rahman, B. Biswas, Md. Farid Ahmed, M. Aftab Ali Shaikh, S. Akter Jahan and N. Sharmin, *J. Ind. Eng. Chem.*, 2023, **126**, 340–359.
46 L. Jabbar and A. Al-Farraji, *Environ. Nanotechnol., Monit. Manage.*, 2022, **18**, 100701.
47 E. S. Elmorsy, W. A. Amer, A. Mahrous and M. M. Ayad, *Mater. Sci. Eng., B*, 2023, **298**, 116900.
48 A. Wang, J. Ni, W. Wang, X. Wang, D. Liu and Q. Zhu, *J. Hazard. Mater.*, 2022, **426**, 128106.
49 P. Attri, P. Garg, M. Chauhan, R. Singh, R. K. Sharma, S. Kumar, D.-K. Lim and G. R. Chaudhary, *J. Environ. Chem. Eng.*, 2023, **11**, 109498.
50 H. Dai, X. Yuan, L. Jiang, H. Wang, J. Zhang, J. Zhang and T. Xiong, *Coord. Chem. Rev.*, 2021, **441**, 213985.
51 H.-P. Jing, C.-C. Wang, Y.-W. Zhang, P. Wang and R. Li, *RSC Adv.*, 2014, **4**, 54454–54462.
52 R. Chandra, S. Mukhopadhyay and M. Nath, *Mater. Lett.*, 2016, **164**, 571–574.
53 F. Naz, C. H. Mak, Z. Wang, H. Tong, S. P. Santoso, M. Du, J.-J. Kai, K.-C. Cheng, C.-W. Hsieh, W. Niu, Z. Hu and H.-Y. Hsu, *RSC Appl. Interfaces*, 2025, **2**, 741–754.
54 S. Vadivel, A. Muthuraj, M. Anbazhagan, S. Abdul samad and R. Arumugam, *Environ. Pollut.*, 2023, **336**, 122450.
55 M. Hu, D. Zhao, X. Yan, X. Hu, M. Zhou, Y. Shu and P. Liu, *Appl. Surf. Sci.*, 2024, **665**, 160321.
56 R. Subagyo, A. R. Diakana, G. R. Anindika, S. Akhlus, H. Juwono, L. Zhang, Arramel and Y. Kusumawati, *ACS Omega*, 2024, **9**, 25251–25264.
57 H. Zheng, D. Wu, Y. Wang, X. Liu, P. Gao, W. Liu, J. Wen and E. V. Rebrov, *J. Alloys Compd.*, 2020, **838**, 155219.
58 J. Cao, Z. Yang, W. Xiong, Y. Zhou, Y. Peng, X. Li, C. Zhou, R. Xu and Y. Zhang, *Chem. Eng. J.*, 2018, **353**, 126–137.
59 M. Samy, M. Gar Alalm, M. Fujii and M. G. Ibrahim, *J. Water Process Eng.*, 2021, **44**, 102449.
60 I. Rabani, S. Patil, M. Tahir, F. Afzal, J.-W. Lee, H. Im, Y.-S. Seo and N. Shrestha, *J. Nanomater.*, 2023, **13**, 1610.